

# Demonstration of complex-conjugate-resolved harmonic Fourier-domain optical coherence tomography imaging of biological samples

Andrei B. Vakhtin,\* Kristen A. Peterson, and Daniel J. Kane

Southwest Sciences, Inc., 1570 Pacheco Street, Suite E-11, Santa Fe, New Mexico 87505, USA

\*Corresponding author: avakhtin@swsciences.com

Received 3 July 2006; revised 12 January 2007; accepted 23 February 2007;  
posted 16 March 2007 (Doc. ID 72573); published 31 May 2007

Complex-conjugate-resolved Fourier-domain optical coherence tomography, where the quadrature components of the interferogram are obtained by simultaneous acquisition of the first and second harmonics of the phase-modulated interferogram, is applied to multisurface test targets and biological samples. The method provides efficient suppression of the complex-conjugate, dc, and autocorrelation artifacts. A complex-conjugate rejection ratio as high as 70 dB is achieved. © 2007 Optical Society of America

*OCIS codes:* 170.4500, 170.3880, 120.3180.

## 1. Introduction

During the past few years, Fourier-domain optical coherence tomography (FD-OCT) has become an attractive alternative to conventional time-domain OCT (TD-OCT) because it has been demonstrated, both theoretically and experimentally, that FD-OCT has the potential to provide better sensitivity and dynamic range than TD-OCT [1–3]. However, a major drawback of FD-OCT that limits its practical use is the complex-conjugate ambiguity, which is inherent to real Fourier transforms. Because of this artifact, an FD-OCT image obtained from a real-valued spectral interferogram is always symmetrical with respect to the zero plane (zero phase delay) of the interferometer. To avoid ambiguity in interpretation of the image, the zero plane must be positioned outside of the imaged sample. Thus, only one half of the imaging depth range is useful in practice. Resolving the complex-conjugate ambiguity would double the imaging depth range and provide additional flexibility by allowing arbitrary positioning of the zero plane, e.g., moving it inside the sample.

One way to eliminate the complex-conjugate artifact in FD-OCT is to obtain the full complex spectral inter-

ferogram. In fact, it is the access to both real and imaginary parts of the spectral interferogram that makes FD-OCT a truly Fourier-transform analog of TD-OCT. In particular, the capability of obtaining the complex interferogram may be essential for the emerging spectroscopically resolved FD-OCT method [4,5]. While TD-OCT, in principle, can provide spectroscopic information in addition to structural information, the full interferogram must be digitized [6]. Full-range FD-OCT can provide equivalent information in a more straightforward way; therefore, this method appears to be the most appropriate for spectroscopic OCT.

The problems of obtaining the full complex interferogram and resolving the complex-conjugate ambiguity in FD-OCT have been addressed using different approaches, including phase-shifting methods [7–10], simultaneous detection of the quadrature components of the interferogram by using  $3 \times 3$  fiber-optic couplers [11,12], separation of the two complex-conjugate images using carrier-frequency shifting in swept-source FD-OCT [13–15], and using polarization-based optical demodulation [16]. Phase-shifting methods [7,8] allow acquisition of the complex spectral interferogram to be obtained in a multiframe sequence; however, in practice the complex-conjugate rejection ratio is limited by accuracy of the phase steps and also by the mechanical stability of the interferometer and the sample during the acquisition time of the frame se-

---

0003-6935/07/183870-08\$15.00/0

© 2007 Optical Society of America

quence [9,10]. Although least-squares algorithms are somewhat helpful in determining the actual phase-step amplitudes [17,18], the rejection of the complex conjugate is usually <40 dB.

Detection of the complex interferogram using  $3 \times 3$  fiber couplers as phase-shifting elements allows simultaneous detection of the real and imaginary components of the spectral interferogram by two separate detectors [11,12]. The reported maximum complex-conjugate rejection ratio is 20 dB for broadband FD-OCT and 25 dB for swept-source FD-OCT [12]. Recently, a rejection ratio of >30 dB has been achieved [19].

Carrier-frequency shifting methods in swept-source FD-OCT separate the two mirror images and resolve the complex-conjugate ambiguity [13–15]. However, these methods are not applicable to parallel FD-OCT (which involves a broadband light source and detection of the spectral interferograms with an array detector).

Another full-range version of swept-source FD-OCT has recently been described, where polarization-based optical demodulation is used [16]. A complex-conjugate rejection ratio of >50 dB has been reported.

Recently we presented a new method of direct acquisition of the complex spectral interferogram [20]. The imaginary and real components are detected simultaneously as the first and second harmonics of a phase-modulated interferogram. The technique is applicable to both parallel and swept-source FD-OCT. By imaging a one-surface sample (a mirror), we demonstrated that the method efficiently removes the dc, autocorrelation, and complex-conjugate artifacts. In that work, sine phase modulation was introduced to the interferometer by dithering the reference mirror with a piezotranslator; however, any other phase modulator could be used. The measured complex-conjugate rejection ratio was at least 45 dB and was limited by the background noise floor. In addition to efficient suppression of the above-mentioned artifacts, the two-harmonic method has the following advantages over the existing full-range FD-OCT techniques: (1) Since the phase is modulated with a pure sine wave, the requirements to the phase-modulating and signal-acquisition electronics are not very demanding (only ac signals at the first and second harmonics of the phase-modulation frequency have to be detected). (2) The real and imaginary parts of the spectral interferogram are acquired simultaneously using the same detector. (3) For a given imaging rate, the detection bandwidth for harmonic detection is similar to standard parallel or swept-source FD-OCT; therefore, no significant reduction in the signal-to-noise ratio is expected.

In this paper we present a more detailed description of the method and the experimental setup and also show complex-conjugate-resolved FD-OCT images of more complex samples including multisurface test targets and a *Xenopus laevis* tadpole. The method is implemented in two ways: (1) using a single detector and scanning monochromator, which can be con-

sidered a slow version of swept-source two-harmonic FD-OCT, and (2) using an integrating array detector coupled to a spectrograph, which serves as a prototype of parallel implementation of the method. For the first time, full-range FD-OCT images of biological samples with complex-conjugate rejection of up to 70 dB are demonstrated.

## 2. Experiment

### A. Experimental Setup

For the two types of proof-of-principle experiments (single detector/scanning monochromator and integrating array detector/spectrograph), two different experimental setups were used.

#### 1. Single-Detector/Scanning Monochromator Implementation (Type I)

The experimental setup is shown in Fig. 1(a). It is based on a free-space Michelson-type interferometer. A Ti:sapphire laser (center wavelength 800 nm, FWHM 27 nm) is used as the light source. The probe light is focused on a sample with a ThorLabs C230TM aspheric single lens. Lateral scanning is performed us-

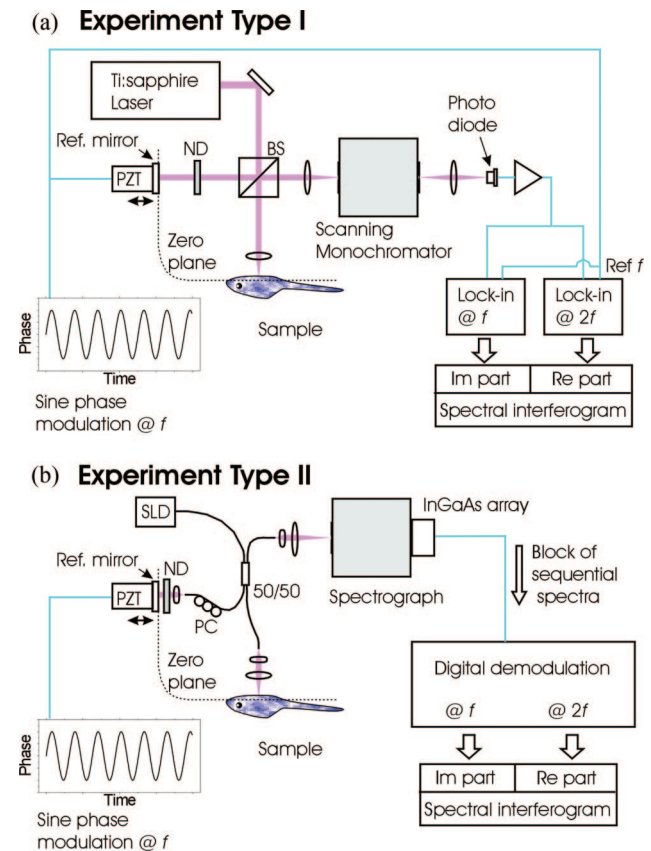


Fig. 1. (Color online) Experimental setups used for demonstration of two-harmonic FD-OCT imaging biological samples. (a) Type I: acquisition of spectral interferograms using a single detector and scanning monochromator. (b) Type II: acquisition of spectral interferograms using an integrating detector array and spectrograph. PZT, piezo translator; ND, neutral-density filter; BS, beam splitter; SLD, super luminescent diode; 50/50, fiber coupler; PC, polarization control.

ing a computer-controlled motorized XY-translation stage. A sine wave (frequency  $f = 1.5$  kHz) produced by the reference sine-wave generator of a Stanford Research Systems SR830 lock-in amplifier is applied to the piezotranslator holding the mirror in the reference arm of the interferometer to introduce phase modulation. The spectral interferograms are obtained using a computer-controlled 1/4-meter scanning monochromator (Chromex; grating 600 lines/mm, resolution 0.3 nm) coupled to a photodiode equipped with a lab-built transimpedance preamplifier. The interferograms consisting of 128 or 256 points and covering the wavelength range of 770–830 nm are acquired in evenly spaced wavenumber domain. For each A-scan, two differential spectral interferograms are detected simultaneously by demodulating the ac-coupled photodiode signal at  $f$  and  $2f$  (time constant 30 ms) using two lock-in amplifiers (Stanford Research Systems, SR830) at each wavelength of the spectral scan. The demodulated signals are transferred to a personal computer through a general-purpose interface bus (GPIB) interface. It takes 7 or 13 seconds to acquire one interferogram (for the 128-point and 256-point spectrum, respectively). As described earlier [20] and discussed in the next subsection, the first and the second harmonics represent the imaginary and the real parts of the complex spectral interferograms, respectively.

## 2. Integrating Array Detector/Spectrograph Implementation (Type II)

The experimental setup is shown in Fig. 1(b). It involves a fiber optic interferometer and a Superlum BroadLighter 1300 superluminescent diode (SLD) light source (center wavelength 1300 nm, FWHM 85 nm). As in the type I experiment, the probe light is focused on a sample with a ThorLabs C230TM lens, lateral scanning is performed using a motorized XY-translation stage, and a sine wave is applied to the piezotranslator holding the reference mirror to phase modulate the interferometer. In this experiment a sine wave of a lower frequency ( $f = 23$  Hz) was used. The spectral interferograms are obtained using a 1/4-meter spectrograph (Oriel 77200, grating 600 lines/mm, resolution 0.3 nm) coupled to an InGaAs integrating array detector (Hamamatsu G9202-512S sensor on a C8061-01 detector head). Normally, a block of 400 spectral interferograms, 512 spectral points each, and covering the wavelength range of 1220–1375 nm, are acquired at a rate of 200 Hz, which takes 2 s. The block of phase-modulated spectra is then converted to evenly spaced wavenumber domain, digitally demodulated at the first and second harmonics of the modulation frequency, and low-pass filtered (time constant 1 s) to yield the real and imaginary components of the complex spectral interferogram.

As a demonstration of applicability of the method to biological samples, we obtained two-harmonic FD-OCT images of fixed *Xenopus laevis* (stage 45) and *Xenopus tropicalis* tadpoles (stage 45).

## B. Two-Harmonic Complex Fourier-Domain Optical Coherence Tomography

In this subsection, the principle of two-harmonic FD-OCT is described. For simplicity, consider FD-OCT imaging of a sample that has only one backscattering surface (e.g., a mirror). The spectral interferogram at the output of a phase-modulated interferometer can be expressed as follows:

$$I_{SI}(\omega, t) = I_R(\omega) + I_S(\omega) + 2[I_R(\omega)I_S(\omega)]^{1/2} \times \cos[\Delta\phi_S(\omega) + \phi_0(\omega, t)], \quad (1)$$

where  $\omega$  is the optical frequency;  $t$  is time;  $I_R(\omega)$  and  $I_S(\omega)$  are the light intensities in the reference and the sample arms of the interferometer, respectively;  $\Delta\phi_S(\omega)$  is the phase delay corresponding to the sample;  $\phi_0(\omega, t)$  is time-dependent phase term that describes phase modulation. With harmonic phase modulation at a frequency  $f$ , the latter term becomes

$$\phi_0(\omega, t) = a_m(\omega)\sin \omega_m t, \quad (2)$$

where  $\omega_m = 2\pi f$ , and  $a_m(\omega)$  is the phase-modulation amplitude. Expanding the last term on the right side of Eq. (1) into a series of Bessel functions ( $J_0, J_1, J_2, \dots$ ) we have

$$I_{SI}(\omega, t) = I_R(\omega) + I_S(\omega) + 2[I_R(\omega)I_S(\omega)]^{1/2} \{ J_0[a_m(\omega)] - 2J_1[a_m(\omega)]\sin \omega_m t \sin \Delta\phi_S(\omega) + 2J_2[a_m(\omega)]\cos 2\omega_m t \cos \Delta\phi_S(\omega) - 2J_3[a_m(\omega)]\sin 3\omega_m t \sin \Delta\phi_S(\omega) + 2J_4[a_m(\omega)]\cos 4\omega_m t \cos \Delta\phi_S(\omega) - \dots \}. \quad (3)$$

As follows from Eq. (3), the signals demodulated at the first ( $H_1$ ) and the second ( $H_2$ ) harmonics of the modulation frequency are

$$H_1[\omega, \Delta\phi_S(\omega)] = -4J_1[a_m(\omega)][I_R(\omega)I_S(\omega)]^{1/2} \times \sin \Delta\phi_S(\omega), \quad (4)$$

$$H_2[\omega, \Delta\phi_S(\omega)] = 4J_2[a_m(\omega)][I_R(\omega)I_S(\omega)]^{1/2} \times \cos \Delta\phi_S(\omega). \quad (5)$$

$H_1$  and  $H_2$  (as any other pair of odd and even harmonics) represent the sine and cosine, i.e., imaginary and real parts of the complex spectral interferogram, respectively. The complex inverse Fourier transform can be applied to the complex interferogram to convert it into the time-domain profile that is free from complex-conjugate ambiguity and also the dc and autocorrelation terms:

$$f(\tau) = \mathfrak{F}^{-1}\{\beta H_2[\omega, \Delta\phi_S(\omega)] - iH_1[\omega, \Delta\phi_S(\omega)]\}. \quad (6)$$

According to Eqs. (4) and (5), the scaling coefficient  $\beta$  is equal to

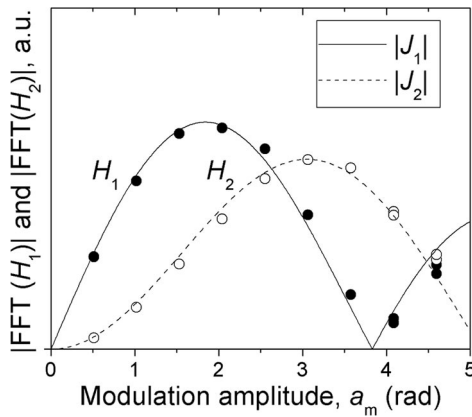


Fig. 2. Points: experimental data on the dependence of the magnitudes of the first- ( $H_1$ ) and second-harmonic ( $H_2$ ) signals on the modulation amplitude. Curves: absolute values of the first- and second-order Bessel functions ( $J_1$  and  $J_2$ ).

$$\beta = J_1[a_m(\omega)]/J_2[a_m(\omega)] \quad (7)$$

and depends only on the modulation amplitude  $a_m$ , which is, generally, wavelength dependent. For example, if the phase modulation is achieved by dithering the reference mirror,  $a_m$  scales linearly with the optical frequency  $\omega$ , which can easily be taken into account during signal acquisition and signal processing, as can any other known wavelength dependence.

We checked experimentally that the dependence of the first- and second-harmonic signals on the modulation amplitude is consistent with Eqs. (4) and (5). In these experiments, a mirror was used as a sample. Figure 2 shows the magnitudes of the Fourier-transformed spectral interferograms obtained by demodulating the phase-modulated interferogram at the first and second harmonics plotted versus the modulation amplitude. The experimental points are well described by the absolute values of the first- and second-order Bessel functions, which confirms the validity of the representation of the scaling coefficient by the  $J_1/J_2$  ratio [Eq. (7)]. Therefore, if the modulation amplitude is known, the scaling coefficient can easily be calculated. Figure 2 also provides some idea of a practically useful range for the modulation amplitude  $a_m$ . Generally, the modulation amplitude should be chosen so that the zeros of the first- and second-order Bessel functions are avoided, and the first- and second-harmonic signals are comparable in magnitude. A range of  $0.8 \leq a_m/\text{rad} \leq 3.5$  is reasonable.

If the modulation amplitude is not known accurately, the scaling coefficient  $\beta$  or the modulation amplitude  $a_m$  can be either treated as an adjustable parameter or obtained independently from the ratio of the first and the third harmonics. In the former method, a single-surface sample that produces a strong signal (e.g., a mirror) is used, and the scaling coefficient is adjusted to maximize the complex-conjugate artifact rejection. This routine is described in more detail below. Alternatively, the measured ratio of the first and third harmonics can be used to

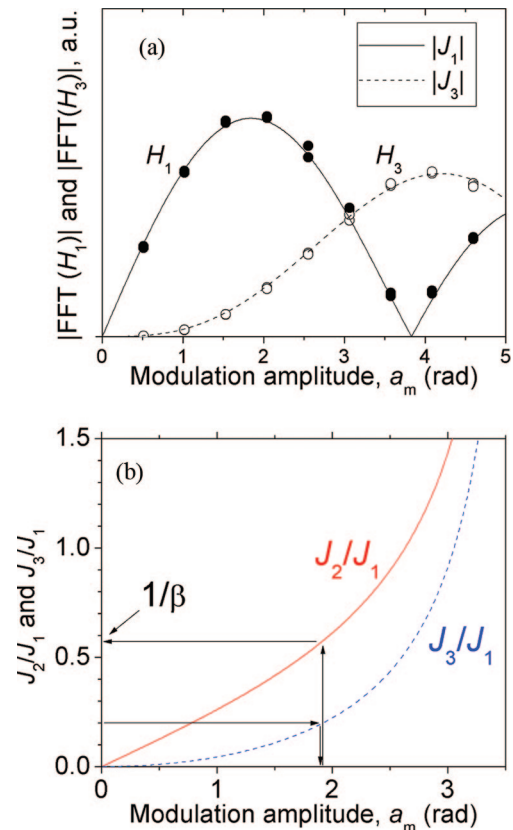


Fig. 3. (Color online) (a) Points: experimental data on the dependence of the magnitudes of the first- ( $H_1$ ) and third-harmonic ( $H_3$ ) signals on the modulation amplitude. Curves: absolute values of the first- and third-order Bessel functions ( $J_1$  and  $J_3$ ). (b) A procedure of determining the modulation amplitude based on the measurement of the  $J_3/J_1$  ratio.

determine the modulation amplitude and  $\beta$ . Figure 3 schematically shows the procedure. Actually, any odd-odd or even-even pair of harmonics can be used to determine the modulation amplitude, since the harmonics of the same parity are related to the same component (real or imaginary) of the complex interferogram.

Generally, it is convenient to treat the  $\beta$  scaling coefficient as an adjustable parameter. The experimental procedure is as follows. First, the initial setup of the instrument has to be performed. It consists of the following steps:

1. With a mirror used as a sample, the interferograms demodulated at the first and the second harmonics are acquired, and the phases are adjusted so that the in-phase component for each of the demodulated signals is maximized.
2. An initial value of  $a_m^0$ , the modulation amplitude at the center optical frequency of the spectral window, is assumed.
3. The modulation amplitudes  $a_m(\omega_i)$  are calculated for each optical frequency  $\omega_i$  of the acquired spectral interferogram. In our case, where the phase modulation is achieved by dithering the reference mirror,  $a_m$  scales linearly with the optical frequency  $\omega$ :

$$a_m(\omega_i) = a_m^0 \omega_i / \omega_0, \quad (8)$$

where  $\omega_0$ , is the center optical frequency of the spectral window.

4. The scaling coefficients  $\beta$  are calculated for each optical frequency  $\omega_i$  of the acquired spectral interferogram as follows:

$$\beta(\omega_i) = J_1(a_m^0 \omega_i / \omega_0) / J_2(a_m^0 \omega_i / \omega_0). \quad (9)$$

5. The inverse complex Fourier transform is applied to the scaled complex interferogram [see Eq. (6)] to obtain the time domain (or depth) profile, the A-scan.

6. From the A-scan, the complex-conjugate artifact rejection ratio is determined.

7. If a satisfactory complex-conjugate rejection ratio is achieved, the initial setup is finished. If not, the sequence starting from step 3 is repeated with a new approximation for  $a_m^0$ .

After the initial setup is complete, the instrument can be used for imaging other samples. The initial setup has to be performed *only once* for a given set of experimental conditions. Once optimized, the array of  $\beta(\omega_i)$  is used for acquisition of complex interferograms for arbitrary samples. Our experience shows that as long as the modulation amplitude, the modulation frequency, and the set of optical frequencies for spectral interferogram acquisition are not changed, it is not necessary to rerun the initial setup.

### 3. Results and Discussion

In this section, FD-OCT images of complex samples obtained using the two-harmonic method of acquiring the complex spectral interferograms are presented. Figure 4 shows a cross-sectional FD-OCT scan of a three-surface test target constructed of a microscope cover slide attached to a mirror through a spacer. The sample is tilted with respect to the probe beam to provide a clear idea of the expected locations of the complex-conjugate image components. The image in Fig. 4(a) is constructed of A-scans obtained by applying the Fourier transform to the complex interfero-

grams acquired using the two-harmonic method, which involves a single photodetector and scanning monochromator (type I experiment, Fig. 1(a)). The modulation amplitude  $a_m^0$  is 0.908 radians, which corresponds to  $\beta^0 = 4.25$  (at the center optical frequency of the spectral window). For comparison, Fig. 4(b) shows the image obtained from the real part of the interferogram, i.e., the image that could be obtained by conventional FD-OCT, which detects real-valued interferograms. The horizontal line marked "zero plane" shows the zero phase delay plane. Figures 4(c) and 4(d) show representative A-scans of this sample obtained using the full complex spectral interferogram and only the real part of the interferogram, respectively. The obtained data show rejection of the complex conjugate down to the background level (up to 45 dB). Note, in Figs. 4(a) and 4(b), the additional lines parallel to the lines representing the three surfaces are not artifacts caused by the method; these ghost images result from multiple reflections between the highly reflective surfaces in the sample.

As an example of imaging a biological sample using the type I implementation of the two-harmonic FD-OCT, Figures 5(a) and 5(b) show transverse FD-OCT scans of the dorsal side of a stage 45 *Xenopus laevis* tadpole obtained using complex-valued and real-valued spectral interferograms, respectively. The modulation amplitude  $a_m^0$  is 0.908 radians, which corresponds to  $\beta^0 = 4.25$ . Figures 5(c) and 5(d) show representative A-scans of the tadpole sample obtained using the full complex spectral interferogram and only the real part of the interferogram. The image data show rejection of the complex-conjugate artifact down to the background level. We did not apply any antialiasing filtering to the interferograms; therefore, some aliasing artifacts can be seen. Images shown in Fig. 4 and Fig. 5 confirm applicability of the two-harmonic FD-OCT method to imaging complex objects. A background-noise-limited complex-conjugate rejection ratio as high as 45 dB, as well as suppression of the dc and autocorrelation artifacts, is achieved.

The overall quality of the images is not very good in these experiments for the following reasons. (1) Be-

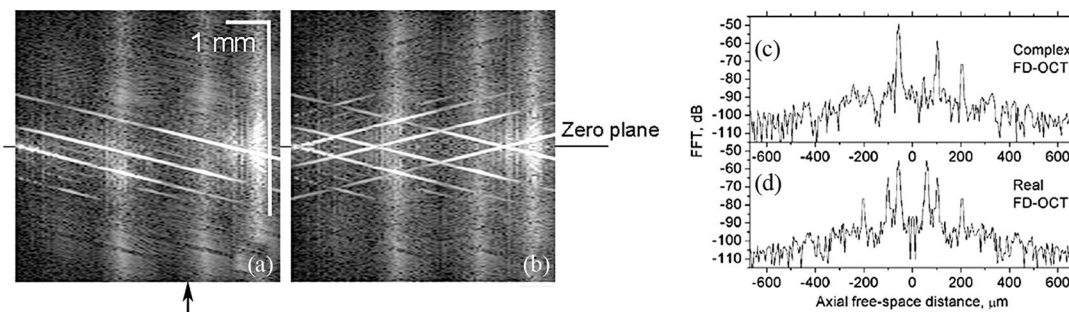


Fig. 4. (a) FD-OCT cross-sectional image of a three-surface sample constructed of a microscope cover slide attached to a mirror through a spacer, obtained using the two-harmonic method of acquisition of the complex interferograms, which involves a single photodetector and scanning monochromator (type I experiment;  $\lambda = 800$  nm;  $a_m^0 = 0.908$  rad,  $\beta^0 = 4.25$ ). Image size: 256 pixels (depth)  $\times$  100 pixels (lateral). (b) FD-OCT image of the same sample obtained using only the real part of the complex interferograms. (c), (d) A-scans indicated by the arrow in (a), obtained using the complex spectral interferogram (c) and using the real part of the spectral interferogram (d).

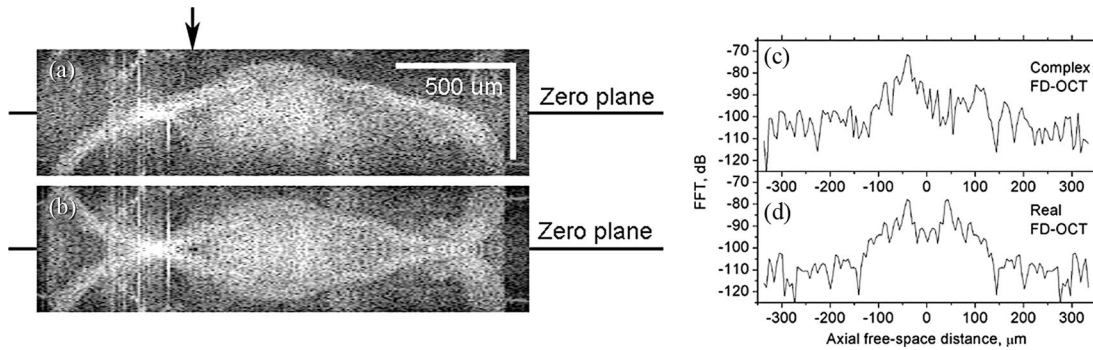


Fig. 5. (a) FD-OCT transverse scan of the dorsal side of a *Xenopus laevis* tadpole (stage 45) obtained using the two-harmonic method of acquisition of the complex interferograms, which involves a single photodetector and scanning monochromator (type I experiment;  $\lambda = 800$  nm;  $a_m^0 = 0.908$  rad,  $\beta^0 = 4.25$ ). Image size: 128 pixels (depth)  $\times$  200 pixels (lateral). (b) FD-OCT image of the same sample obtained using only the real part of the complex interferograms. (c), (d) A-scans indicated by the arrow in (a), obtained using the complex spectral interferogram (c) and using the real part of the spectral interferogram (d).

cause of the slow data acquisition with the current setup, only relatively small images can be obtained in a reasonably short period of time. For example, the tadpole images are only  $128 \times 200$  pixels. (2) As shown earlier [20], the slow sequential point-by-point acquisition of the spectral interferograms used in this experiment is very sensitive to the low-frequency phase noise, which results in a broad noise pedestal affecting the image. Faster data acquisition is needed to improve the image quality. Nevertheless, even with the present slow data acquisition, the images obtained from the complex interferograms shown in Figs. 4 and 5 exhibit no signs of the complex conjugate, dc, or autocorrelation artifacts. Although the dynamic range is not very high, the rejection ratio for these artifacts is high enough to suppress them to the level of the background noise floor. This slow data-acquisition method was used for demonstration purposes and is analogous to swept-source OCT (the detection wavelength is varied instead of the source wavelength). With faster, swept-source instrumentation, improved dynamic range and rejection ratio are expected.

Figure 6 shows FD-OCT transverse images of region of a *Xenopus tropicalis* tadpole head obtained using a 1300 nm SLD light source and InGaAs integrating array detector coupled to a spectrograph [type II experiment, Fig. 1(b)]. The zero plane is placed slightly below the dorsal (top) surface of the tadpole's head. The modulation amplitude  $a_m^0$  is 2.77 radians, which corresponds to  $\beta^0 = 0.88$ . The images shown in Figs. 6(a) and 6(b) are obtained using the full complex interferograms and only the real interferogram, respectively. The eyes, optic nerves, brain, and other features of the internal structure of the animal are clearly visible. In Fig. 6(a) the complex-conjugate image is suppressed to the background noise level and is not visible at all. The only exception is the very bright image of the eye on the right side of the image, for which a weak complex-conjugate artifact remains. Figure 7 shows representative examples of A-scans that correspond to that area [indicated with arrows in Fig. 6(a)]. The complex-

conjugate rejection ratio is typically 50–60 dB, and can be as low as 40 dB and as high as 70 dB. We attribute the incomplete rejection, as well as incompletely suppressed dc artifact at the zero phase delay in the tadpole image, to the slow 0.5 Hz A-scan data

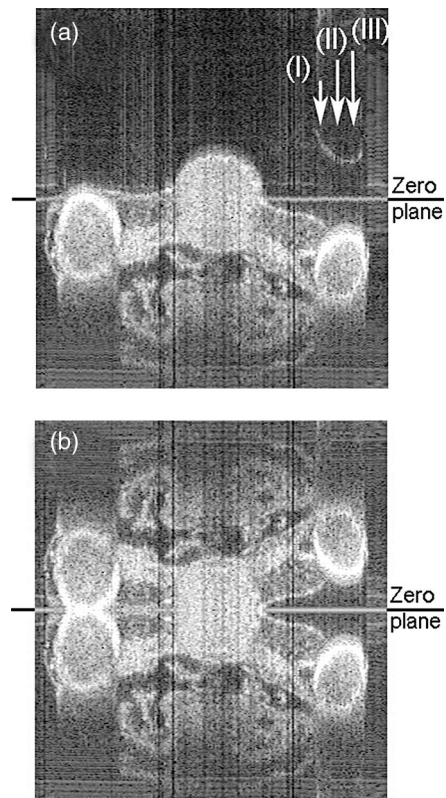


Fig. 6. (a) FD-OCT transverse scan of the dorsal side of a *Xenopus tropicalis* tadpole (stage 45) obtained using the two-harmonic method of acquisition of the complex interferograms, which involves an InGaAs integrating array detector coupled to a spectrograph (type II experiment;  $\lambda = 1300$  nm;  $a_m^0 = 2.77$  rad,  $\beta^0 = 0.88$ ). Image size: 380 pixels (2 mm), depth  $\times$  200 pixels (1.5 mm), lateral. Arrows indicate the A-scans shown in Fig. 7. (b) FD-OCT image of the same sample obtained using only the real part of the complex interferograms.

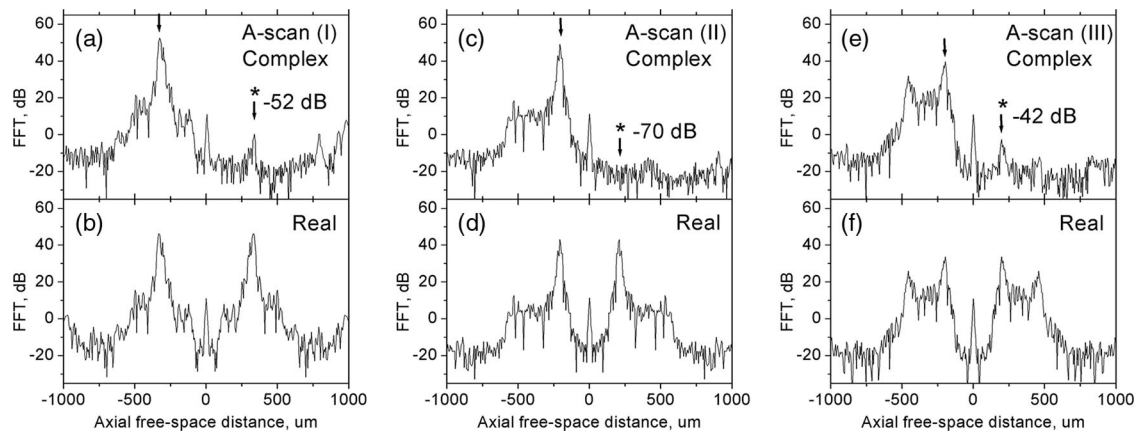


Fig. 7. A-scans indicated by arrows in Fig. 6(a): (a), (b) A-scan (I); (c), (d) A-scan (II); (e), (f) A-scan (III). A-scans (a), (c), and (e) are obtained using the complex spectral interferograms. A-scans (b), (d), and (f) are obtained using the real part of the spectral interferograms. On plots (a), (c), and (e), arrows indicate the strongest peak and its complex conjugate. The complex-conjugate rejection ratios are listed. Small, residual dc peaks are visible at zero depth.

acquisition used in this experiment in conjunction with the low-frequency phase noise that is inherent to the fiber-optic interferometer. (The dc term is fully rejected when the free-space interferometer is used; see Figs. 4 and 5.) With this type of experiment we also expect that improvement can be achieved by using faster data acquisition.

In summary, we present images of a multisurface test target and tadpoles, which prove applicability of our recently developed two-harmonic complex FD-OCT method to biological samples. The complex-conjugate, dc, or autocorrelation artifacts are rejected to (or close to) the background noise level. Complex-conjugate rejection ratios of up to 70 dB are achieved in full-range imaging of biological samples. Although the presented results are obtained using slow, proof-of-principle prototypes of swept-source and parallel two-harmonic FD-OCT, we believe that transition to high-speed implementation of both versions of the method is straightforward. In particular, with parallel FD-OCT, one option is implementing the type II scheme [Fig. 1(b)] using a high-speed integrating array detector, such as a linescan camera. Another option is using a custom demodulating array detector. Experimental work on investigation of both possibilities is currently in progress. We believe our method will be useful for a variety of biomedical low-coherence optical imaging applications, including spectroscopic FD-OCT.

This work was supported by the National Institute of Health under grant 1 R43 HL079781-01. We thank Elba E. Serrano of New Mexico State University for providing the fixed *Xenopus* tadpoles.

## References

1. R. A. Leitgeb, C. K. Hitzenberger, and A. F. Fercher, "Performance of Fourier domain versus time domain optical coherence tomography," *Opt. Express* **11**, 889–894 (2003).
2. M. A. Choma, M. V. Sarunic, C. Yang, and J. A. Izatt, "Sensitivity advantage of swept source and Fourier domain optical coherence tomography," *Opt. Express* **11**, 2183–2189 (2003).
3. J. F. de Boer, B. Cense, B. H. Park, M. C. Pierce, G. J. Tearney, and B. E. Bouma, "Improved signal-to-noise ratio in spectral-domain compared with time-domain optical coherence tomography," *Opt. Lett.* **28**, 2067–2069 (2003).
4. R. Leitgeb, M. Wojtkowski, A. Kowalczyk, C. K. Hitzenberger, M. Sticker, and A. F. Fercher, "Spectral measurement of absorption by spectroscopic frequency-domain optical coherence tomography," *Opt. Lett.* **25**, 820–822 (2000).
5. C. Xu, C. Vinegoni, T. S. Ralston, W. Luo, W. Tan, and S. A. Boppart, "Spectroscopic spectral-domain optical coherence tomography," *Opt. Lett.* **31**, 1079–1081 (2006).
6. U. Morgner, W. Drexler, F. X. Kartner, X. D. Li, C. Pitris, E. P. Ippen, and J. G. Fujimoto, "Spectroscopic optical coherence tomography," *Opt. Lett.* **25**, 111–113 (2000).
7. P. Hariharan, B. F. Oreb, and T. Eiju, "Digital phase-shifting interferometry: a simple error-compensating phase calculation algorithm," *Appl. Opt.* **26**, 2504–2506 (1987).
8. J. Schmit and K. Creath, "Extended averaging technique for derivation of error-compensating algorithms in phase-shifting interferometry," *Appl. Opt.* **34**, 3610–3619 (1995).
9. M. Wojtkowski, A. Kowalczyk, R. Leitgeb, and A. F. Fercher, "Full range complex spectral optical coherence tomography technique in eye imaging," *Opt. Lett.* **27**, 1415–1417 (2002).
10. R. A. Leitgeb, C. K. Hitzenberger, A. F. Fercher, and T. Bajraszewski, "Phase-shifting algorithm to achieve high-speed long-depth-range probing by frequency-domain optical coherence tomography," *Opt. Lett.* **28**, 2201–2203 (2003).
11. M. A. Choma, C. Yang, and J. A. Izatt, "Instantaneous quadrature low-coherence interferometry with  $3 \times 3$  fiber-optic couplers," *Opt. Lett.* **28**, 2162–2164 (2003).
12. M. V. Sarunic, M. A. Choma, C. Yang, and J. A. Izatt, "Instantaneous complex conjugate resolved spectral domain and swept-source OCT using  $3 \times 3$  fiber couplers," *Opt. Express* **13**, 957–967 (2005).
13. J. Zhang, J. S. Nelson, and Z. Chen, "Removal of a mirror image and enhancement of the signal-to-noise ratio in Fourier-domain optical coherence tomography using an electro-optic phase modulator," *Opt. Lett.* **30**, 147–149 (2005).
14. S. H. Yun, G. J. Tearney, J. F. de Boer, and B. E. Bouma, "Removing the depth-degeneracy in optical frequency domain imaging with frequency shifting," *Opt. Express* **12**, 4822–4828 (2004).
15. A. M. Davis, M. A. Choma, and J. A. Izatt, "Heterodyne swept-source optical coherence tomography for complete complex

- conjugate ambiguity removal," *J. Biomed. Opt.* **10**, 064005 (2005).
16. B. J. Vakoc, S. H. Yun, G. J. Tearney, and B. E. Bouma, "Elimination of depth degeneracy in optical frequency-domain imaging through polarization-based optical demodulation," *Opt. Lett.* **31**, 362–364 (2006).
  17. G.-S. Han and S.-W. Kim, "Numerical correction of reference phases in phase-shifting interferometry by iterative least-squares fitting," *Appl. Opt.* **33**, 7321–7325 (1994).
  18. P. Targowski, I. Gorczynska, M. Szkulmowski, M. Wojtkowski, and A. Kowalczyk, "Improved complex spectral domain OCT for *in vivo* eye imaging," *Opt. Commun.* **249**, 357–362 (2005).
  19. M. V. Sarunic, B. E. Applegate, and J. A. Izatt, "Real-time quadrature projection complex conjugate resolved Fourier domain optical coherence tomography," *Opt. Lett.* **31**, 2426–2428 (2006).
  20. A. B. Vakhtin, K. A. Peterson, and D. J. Kane, "Resolving the complex conjugate ambiguity in Fourier domain OCT by harmonic lock-in detection of the spectral interferogram," *Opt. Lett.* **31**, 1271–1273 (2006).